Polyhedron 91 (2015) 59–67

Contents lists available at ScienceDirect

Polyhedron

journal homepage: www.elsevier.com/locate/poly

Molecular structure, bonding analysis and redox properties of transition metal–Hapca [bis(3-aminopyrazine-2-carboxylic acid)] complexes: A theoretical study

Nora Benhamada [b], Rafika Bouchene [a], Sofiane Bouacida [b], Bachir Zouchoune [a,b,*]

[a] Laboratoire de Chimie appliquée et Technologie des Matériaux, Université Larbi Ben M'Hidi-Oum el Bouaghi, (04000) Oum el Bouaghi, Algeria
[b] Unité de Recherche de Chimie de l'Environnement et Moléculaire Structurale (CHEMS), Université-Constantine 1 (ex Mentouri-Constantine), Algeria

ARTICLE INFO

Article history:
Received 2 October 2014
Accepted 19 December 2014
Available online 10 January 2015

Keywords:
Electronic structure
Bonding analysis
Ionization potential
Electron affinity
Natural bond analysis

ABSTRACT

Density functional theory (DFT) calculations were carried out on $M(Hapca)_2(H_2O)_2$ (M = Mn, Fe, Co, Ni and Hapca = bis(3-aminopyrazine-2-carboxylic acid) by means of the BP86 and B3LYP functional using the TZP basis set. The optimized structures were obtained by imposing C_2 or C_i symmetries. The C_i structural arrangement consists of a slightly distorted octahedron centered by a transition-metal with bidentate Hapca ligands situated in equatorial positions and water molecules in axial ones. However, the C_2 structure consists of a distorted arrangement with *n* con-planar Hapca ligands. The influence induced by including double polarized functions in the (TZ2P) basis set is small on the geometrical parameters. A bonding analysis of these species showed the weakness of M–O(H_2O) bonds compared to M–O(Hapca) ones. The obtained MO diagrams showed substantial HOMO–LUMO gaps for the 18-MVE closed-shell configuration. Reduction of $M(Hapca)_2(H_2O)_2$ led to the loss of the two water molecules, inducing four electrons downwards for **[Co]**$^-$ and **[Ni]** species. The calculated ionization potentials (IPs) and electronic affinities (EAs) showed the oxidation and reduction ease of the manganese species contrarily to the cobalt ones. A diffuse function in the basis set (QZ3P-*n*diffuse, *n* = 1 or 2) reduces remarkably the adiabatic electron affinities (AEAs).

1. Introduction

The most common type of transition metal complex is ML_6, which adopts an octahedral coordination geometry. The ligands occupy the six vertices of the octahedron, which allows them to minimize their M–L bonding distances, while maximizing their L···L non-bonding distances. Chelation is of great interest because it not only makes the complex more stable but also forces the donor atoms to take up adjacent or *cis* sites in the resulting complex. The current work consists of studying bidentate complexes of the general formula $ML_2(H_2O)_2$ (L = 3-aminopyrazine-2-carboxylic acid, Hapca). 3-Aminopyrazine-2-carboxylic acid (Hapca) has received attention recently as a good building block for the construction of novel metal–organic hybrid materials. Multifunctional N and O coordination sites and the ability of the uncoordinated $-NH_2$ group for post-synthetic approaches [1] are the attractive features of the Hapca ligand that allow chelation with metal ions and facilitate the formation of supramolecular architectures [2,3]. Such ligands most commonly donate both lone pairs to the same metal to give a ring compound, and as such are known to be much less easily displaced from a complex than are monodentate ligands of the same category. It is worth noting that organic ligands containing N and O donors give rise to great potential for fine control over coordination structural arrangements [4–10].

Dynamic studies of (Hapca) by inelastic and incoherent neutron scattering, Raman spectroscopy and ab initio calculations have been reported [11]. Hapca is a rigid ligand with O and N atoms that have merits of scarce conformational transformations. Additionally, it can be chosen because the carboxylate group can be deprotonated to provide apca-, thus, affording various acidities depending on the coordination modes. Structural studies of divalent metal ion complexes with the Hapca ligand have shown that the Ni(II) structure consist of $ML_2(H_2O)_2$ monomers, and $ML_2(H_2O)_2{\cdot}H_2O$ is obtained for the Mn(II) complex. In the Mn(II) and Co(II) complexes, the ligand adopts a *cis*-configuration, where the two bidentate Hapca ligands are not coplanar [12], while in the

* Corresponding author at: Laboratoire de Chimie appliquée et Technologie des Matériaux, Université Larbi Ben M'Hidi-Oum el Bouaghi, (04000) Oum el Bouaghi, Algeria. Tel.: +213 6 62038183; fax: +213 32 423983.
E-mail address: b.zouchoune@univ-oeb.dz (B. Zouchoune).

http://dx.doi.org/10.1016/j.poly.2014.12.042
0277-5387/

Ni(II) complex, the chelating bidentate Hapca ligands occupy four equatorial positions of the complex in a *trans*-configuration, while the axial positions are occupied by the monodentate water molecule ligands, coordinated through their oxygen atoms [13].

Pyrazole-3,5-dicarboxylic acid (H_3pdc) features similar N,O-chelating with Ca, Ba and Sr cations and has been widely used to synthesize various coordination polymers because it has very flexible coordination modes [14]. Also, the N,O-chelating mode, forming a six-membered ring with Mn and Cd metals, is observed in $[Mn(H_2dcbi)_2(H_2O)_2]$ and $[Cd(H_2dcbi)_2(H_2O)_2]$ for complexes of the 4,5-dicarboxyimidazole acid (H_3dcbi) ligand [15,16]. Various coordination modes of $H_n$dcbi, ranging from monodentate to μ_5, have been detected. An investigation shows that the singly deprotonated H_2dcbi generally coordinates in the monodentate imidazole-N or N,O-chelate mode, resulting in mononuclear structures [17]. N,O-bidentate ligands are often used to prepare model compounds, based on an understanding of the coordination sphere of the metal centers [18].

In this current study we attempt to give an accurate description of the electronic structure, the molecular bonding and the redox properties of a series of the real compounds $M(Hapca)_2(H_2O)_2$ (M = Mn, Co and Ni) and the hypothetical (M = Fe) type compound, in accordance with the transition metal nature and its oxidation state, by means of density functional theory (DFT) calculations. Thus, the nature of the metal–ligand bonding is analyzed in neutral and ionic species as a function of the total number of metal valence electrons (MVE) and the spin state. A full rationalization has been done to establish their stability according to the molecular symmetry and to compare the results with the available experimental data. To the best of our knowledge, the redox properties of this category of complexes have not been explored elsewhere. Thus, the ionization potential (IP) and the electronic affinity (EA) were analyzed in order to give a deeper insight into the redox properties of the investigated complexes. Quantum chemical calculations of electrochemical redox potentials has become a vastly growing research area.

The reliability of the density functional theory (DFT) model using a non-local density approximation (NLDA) with BP86, which combines Becke's 1988 exchange functional (B) with Perdew's 1986 gradient corrected correlation functional method and the B3LYP functional, has already been established to be valuable in determining electronic structures, geometrical parameters, bonding analysis and other properties from previous theoretical works on mono-metallic complexes [19–26] and related systems [27], and have been shown to reproduce efficiently the experimental structures, though the results always remain dependent upon the level of theory and the used basis set. In order to calibrate the TZP basis set for calculating the geometrical parameters, a double polarized TZ2P basis set has been used.

2. Results and discussion

2.1. Manganese complexes

The $Mn(Hapca)_2(H_2O)_2$ structure has been synthesized in aqueous solution and characterized by single crystal X-ray diffraction, consisting of a distorted octahedral geometry [12] in which the Mn(II) cation is surrounded by two N and two O atoms of Hapca ligands and two O atoms of water molecules. The two Hapca ligands are not coplanar, but they are symmetrically related by a C_2 axis. The full geometry optimizations of the C_i and C_2 symmetries were carried out on the neutral $Mn(Hapca)_2(H_2O)_2$ complex, having 17-MVE in the doublet spin state, there are no differences with respect to the relative energies, as shown in Fig. 1 and Table 1. The C_i structure is slightly more stable than that obtained for the C_2 symmetry, but only by 1.8 kcal/mol (BP86) or 7.5 kcal/mol (B3LYP). The small energy difference, particularly obtained by (BP86) method, is traduced by comparing the bond distances and valence angles (Table 1). For both the C_i and C_2 structures, the Mn–O_1(H_2O) bond lengths of 2.139 and 2.160 Å (BP86) or 2.148 and 1.980 Å (B3LYP), respectively, are similar to the experimental ones of 2.149 Å, while the Mn–O_3(Hapca) bond lengths of 1.990 and 1.940 Å (BP86) or 1.985 and 1.952 Å (B3LYP) are shorter than the experimental value of 2.170 Å. However, the M–N bond lengths are 1.981 and 1.962 Å (BP86) or 2.013 and 2.011 Å (B3LYP) for the C_i and C_2 structures, respectively, showing a discrepancy of the B3LYP results, inversely BP86 gives values comparative to the experimental of 1.988 Å. For the C_i structure, the O_1–Mn–O_2 angle is linear, but for C_2 structure, it is strongly bent, at 97° (BP86) or 95° (B3LYP), and the two Hapca ligands are not coplanar, situated at 81° to each other. The calculated bond distances obtained by the TZ2P basis set are given between brackets in Table 1. One can observe the moderate influence on the bond distances, where the Mn–N distances are slightly lengthened by a value that does not exceed 0.02 Å, inversely the Mn–O_3(Hapca) distance of 2.089 is slightly lengthened by about 0.14 Å, getting closer to the experimental value of 2.170 Å, whilst the Mn–O_1(H_2O) distance is slightly shorter than that obtained by TZP basis set, going from 2.160 to 2.154 Å (C_2 symmetry), but remains comparable to the experimental one of 2.149 Å. The TZ2P basis set gives rise to small changes; thus we can conclude that the results are satisfactory at the TZP level of calculation.

The HOMO (87%) and HOMO−1 (91%) are purely metallic, while the LUMO is principally a ligand (91%) orbital, as sketched in Fig. 2. It is worth noting the non-participation of the water molecules in these crucial orbitals. Accordingly, oxidation and reduction of the neutral compound should not affect the molecular structure.

In order to provide a better understanding of the redox properties of neutral manganese Mn(II) complexes, we have carried out

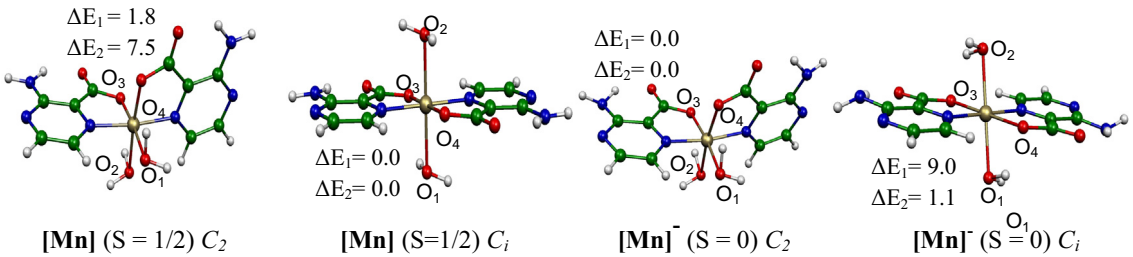

Fig. 1. Optimized **[Mn]**$^+$ and **[Mn]**$^-$ molecular structures with C_i and C_2 symmetries. The relative energies between isomers, ΔE_1 and ΔE_2 (kcal/mol), are obtained by BP86 and B3LYP, respectively.

Table 1
Selected parameters for the **[Mn]** and **[Mn]**$^-$ complexes. The relative energies ΔE_1 (BP86/TZP) and ΔE_2 (B3LYP/TZP) are given in kcal/mol. Values between parentheses are obtained from B3LYP/TZP calculations. The bold values correspond to the experimental bond distances, while the values between brackets are those obtained by BP86/TZ2P.

	[Mn]		[Mn]$^-$			
Spin state	$S = 1/2$		$S = 0$		$S = 1$	
Symmetry	C_2	C_i	C_2	C_i	C_2	C_i
ΔE_1	1.8	0.0	0.0	9.0	3.2	12.6
ΔE_2	(7.5)	(0.0)	(0.0)	(1.1)	(12.3)	(16.7)
HOMO–LUMO (eV)	–	–	0.58	0.27	–	–
	–	–	(2.20)	(1.60)	–	–
Mn–N (Å)	1.962	1.981	1.920	1.951	1.952	1.970
	[1.971]	[1.973]	[1.934]	(1.943)	(1.967)	(1.985)
	(2.011)	(2.013)	(1.930)			
	1.988					
Mn–O_3 (Å)	1.940	1.990	2.031	2.080	1.952	1.931
	[2.089]	[2.076]	[2.007]	(2.088)	(1.970)	(194.2)
	(1.952)	(1.985)	(2.053)			
	2.170					
Mn–O_1 (Å)	2.160	2.139	2.210	2.160	2.194	2.215
	[2.154]	[2.156]	[2.199]	(2.176)	(2.204)	(2.220)
	(1.980)	(2.148)	(2.229)			
	2.149					

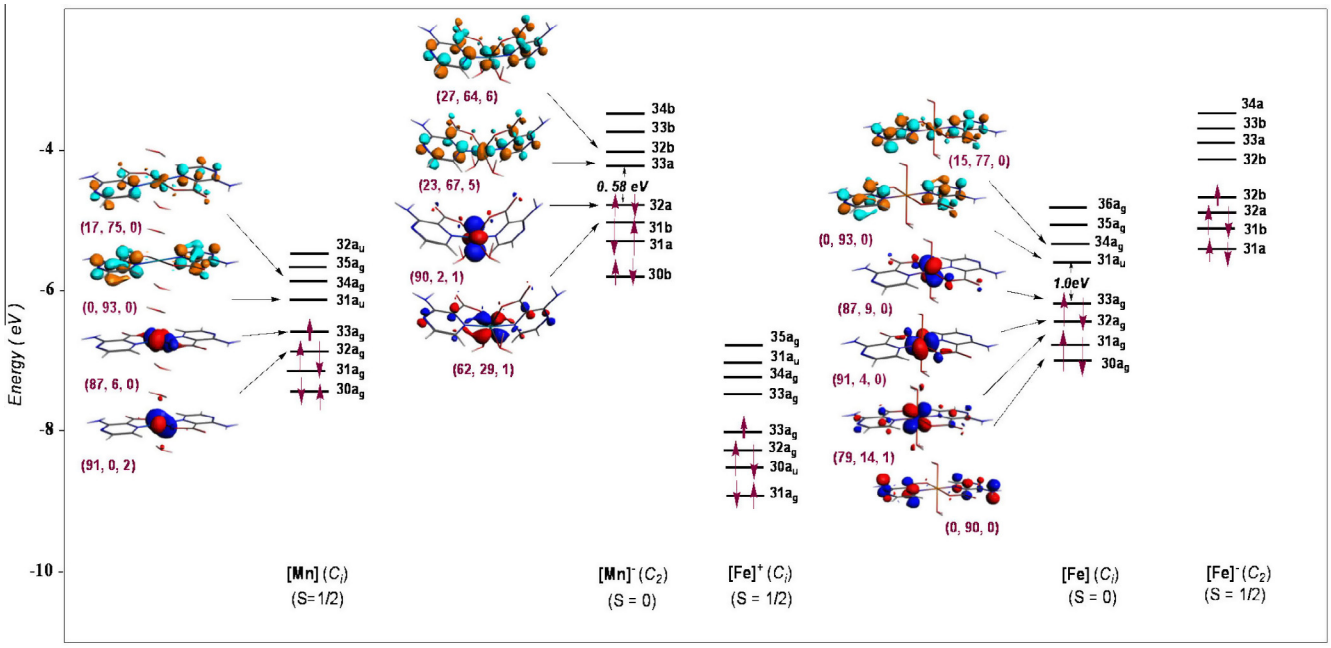

Fig. 2. MO diagrams for **[Mn]** (C_i), **[Mn]**$^-$ (C_2), **[Fe]**$^+$ (C_i), **[Fe]** (C_i) and **[Fe]**$^-$ (C_2) structures. Contour plots ±0.06 e/Bohr^3.

DFT calculations on the reduced **[Mn]**$^-$ form. Selected computed data for the reduced **[Mn]**$^-$ model are given in Table 1 and the optimized geometries are given in Fig. 1. They do not show significant variations between the neutral and the reduced species. Indeed, the global minimum of the reduced model was found to be a singlet spin state of C_2 symmetry, calculated to be more stable than its corresponding triplet spin state by 3.2 kcal/mol for the same symmetry and more stable by 9.0 and 12.6 kcal/mol than those of the singlet and triplet spin states of the C_1 symmetry, respectively, obtained by BP86. The same tendencies are obtained from the B3LYP method, as shown in Table 1. For the **[Mn]** and **[Mn]**$^-$ structures, there is no significant difference between the optimized geometrical parameters. One can observe the same tendencies regarding the various bond lengths and valence angles obtained by both BP86 and B3LYP methods. There is a lengthening of the Mn–O(Hapca) and Mn–O(H_2O) bond distances and the slight shortening of the Mn–N bond distances by about 0.04 Å with respect to population of the SOMO "$33a_g$" by one-electron, which becomes the HOMO of the **[Mn]**$^-$ reduced species. This one-electron reduction of the SOMO "$33a_g$" is accompanied by a natural charge diminution of the metal cation, downwards from +1.08 to +0.65 as determined by Natural Bond Orbital (NBO) analysis [28] (with NBO 5.0 program) [29], emphasizing a considerable gain of 0.43e by the metal (Supplementary information), in agreement with the reduced Mn(I) form, leading to the Mn(II)/Mn(I) redox couple.

2.2. Iron complexes

To the best of our knowledge, the Fe(Hapca)$_2$(H_2O)$_2$ complex has not been obtained experimentally, contrary to the Mn, Co and Ni structures which have been identified by X-ray diffraction

[12,13]. DFT calculations with the BP86 and B3LYP functionals using the same TZVP basis set were performed on the neutral $Fe(Hapca)_2(H_2O)_2$ compound, labeled **[Fe]**, and its oxidized **[Fe]**$^+$ and reduced **[Fe]**$^-$ forms. The optimized geometries of the neutral **[Fe]** compound and its derivatives of C_i and C_2 symmetries are presented in Fig. 3 and their structural data are gathered in Table 2. The obtained findings for **[Fe]** show comparative results, where the energy difference does not exceed 1.0 kcal/mol (BP86) or 4.9 kcal/mol (B3LYP), exhibiting large HOMO–LUMO gaps of 1.10 eV and 1.34 eV (BP86) or 3.1 and 3.2 eV (B3LYP) for the C_i and C_2 structures, respectively, in agreement with the 18-electron configuration as depicted in Fig. 2. A Mulliken population analysis of the MO plots for the C_i structure shows that the three highest HOMO "$33a_g$" (87%), HOMO−1 "$32a_g$" (91%) and HOMO−2 "$31a_g$" (79%) MOs, so-called "t_{2g}" components, are mainly metallic in character, as presented in Fig. 2. However, the LUMO "$31a_u$" is chiefly a ligand orbital (93%), thus the reduction of **[Fe]** should not affect its molecular structure. However, in this case the calculated Fe–$O_1(H_2O)$ bond distances of 2.059 and 2.120 Å (BP86) or 2.063 and 2.100 Å (B3LYP) are longer than those of Fe–O_3(Hapca), 1.986 and 1.962 Å (BP86) or 1.975 and 1.960 Å (B3LYP), while the calculated M–N bond lengths undergo a slight shortening. As said earlier, no experimental structures are available for iron to be compared with our findings. The bond distance changes between TZP and TZ2P are not remarkable, the obtained differences not exceeding 0.06 Å. The NBO analysis attributes a natural charge of +0.82 for the Fe(II) cation, putting emphasis on strong interactions between the metal center and its surround ligands.

We have optimized the geometries of the oxidized **[Fe]**$^+$ model of the C_2 and C_i symmetries in the doublet spin state (Fig. 3). Both isomers were found to be almost isoenergetic, their energy difference being lower than 1.0 kcal/mol (BP86) or 3.9 kcal/mol (B3LYP), values which are not significant at the considered level of theory (Table 2). Furthermore, a careful analysis of their electronic structures indicated almost identical characteristics. The optimized bond distances obtained for **[Fe]**$^+$ of C_2 and C_i structures by both methods are comparable and do not deviate by more than 0.02 Å, except for the Fe–$O_1(H_2O)$ bond distances which are longer for the C_2 structure than the C_i one by 0.08 Å (BP86) and 0.05 Å (B3LYP), as shown in Table 2. The one-electron oxidation induces remarkable Fe–O shortening and slight Fe–N lengthening.

The oxidation of the neutral **[Fe]**, giving rise to the oxidized **[Fe]**$^+$, involves the removal of one-electron from HOMO "$33a_g$" (see Fig. 2), which is computed to be 87% iron based. Accordingly, the NBO analysis gives a value of +1.35 as the Fe

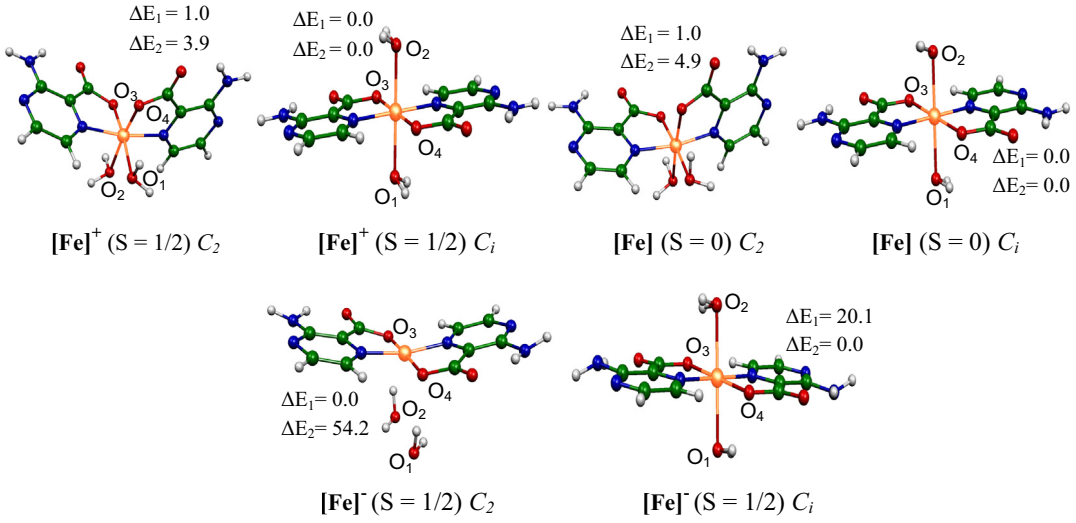

Fig. 3. Optimized **[Fe]**$^+$, **[Fe]** and **[Fe]**$^-$ molecular structures with C_i and C_2 symmetries. The relative energies between isomers, ΔE_1 and ΔE_2 (kcal/mol), are obtained by BP86 and B3LYP, respectively.

Table 2
Selected parameters for the **[Fe]**$^+$, **[Fe]** and **[Fe]**$^-$ complexes. The relative energies ΔE_1 (BP86/TZP) and ΔE_2 (B3LYP/TZP) are given in kcal/mol. Values between parentheses are obtained from B3LYP/TZP calculations. The values between brackets are those obtained by BP86/TZ2P.

Spin	[Fe]$^+$ S = 1/2		[Fe] S = 0		[Fe]$^-$ S = 1/2	
Symmetry	C_2	C_i	C_2	C_i	C_2	C_i
ΔE_1	1.0	0.0	1.0	0.0	0.0	20.1
ΔE_2	(3.9)	(0.0)	(4.9)	(0.0)	(54.2)	(0.0)
HOMO–LUMO (eV)	–	–	1.34	1.01	–	–
	–	–	(3.58)	(3.39)	–	–
Fe–N (Å)	1.991	1.980	1.942	1.941	1.901	1.923
	[1.990]	[1.976]	[1.938]	[1.940]	[1.910]	[1.905]
	(2.008)	(1.986)	(1.997)	(1.978)	(2.011)	(1.923)
Fe–O (Å)	1.850	1.891	1.9621.86	1.986	1.953	2.001
	[1.850]	1.976	(1.96)	[1.981]	[1.950]	[1.950]
	(1.834)	(1.867)		(1.975)	(1.953)	(1.939)
Fe–O_1 (Å)	2.110	2.033	2.121	2.059	3.460	2.081
	[2.123]	[2.032]	[4.420]	[2.052]	[4.440]	[5.436]
	(2.069)	(2.015)	(2.100)	(2.063)	(2.152)	(5.750)

natural charge, showing a loss of 0.43e (Supplementary information). The enhancement of the oxidation state of the iron metal in the **[Fe]**$^+$ species is in accordance with the existence of the Fe(II)/Fe(III) redox couple.

The calculated spin densities of 1.230 and 1.180 (BP86) or 0.91 and 0.93 (B3LYP) for the C_i and C_2 structures (Supplementary information), respectively, clearly show the localization of the unpaired electron on the metal of the oxidized doublet spin state of the **[Fe]**$^+$ species. The one electron attachment to a neutral closed-shell molecule, leading to an open-shell anion is the most difficult case for electron affinity calculations using DFT methods [30]. This corresponds to the iron case, which requires more energy. This attachment corresponds to the population of the LUMO of the neutral **[Fe]** species described above. It is interesting to notice the discrepancy of the obtained results by the BP86 and B3LYP methods. Indeed, for the reduced **[Fe]**$^-$ species, BP86 indicates the C_2 structure is more stable than the C_i one by 20.1 kcal/mol, inversely to this, B3LYP indicates the C_i structure is more stable than the C_2 one by 30.2 kcal/mol. This remarkable difference is traduced by the geometrical parameters. It is worth noting that for each of the most stable conformers obtained by the two methods, water molecules are not connected to the metal, giving rise to deficient 15-MVE species as shown in Fig. 3.

2.3. Cobalt complexes

The structure of $Co(Hapca)_2(H_2O)_2$, designated as **[Co]**, has been characterized by X-ray diffraction by Bouacida and co-workers [31]. The molecular structure consists of a distorted octahedral geometry, where each bidentate Hapca ligand is coordinated to the central Co(II) cation through N and O atoms, and to which two water molecules are added to complete the metallic sphere's coordination. The full geometry optimizations of the C_i and C_2 symmetries were performed on the neutral $Co(Hapca)_2(H_2O)_2$ complex, with 19-MVE in its doublet spin state, which do not show any energy differences. Indeed, it turned out that the C_2 conformation was found to be less stable than the C_i one by 9.8 kcal/mol (BP86) or 6.5 kcal/mol (B3LYP). The difference in energy (B3LYP) is traduced by the bond distances and valence angles differences, where the obtained Co–$O_1(H_2O)$ bond length of 2.410 Å for the C_i symmetry is much longer than that obtained for C_2 symmetry, 2.230 Å. For this neutral species, the spin density is localized exclusively on the cobalt atom, witnessed by values of 0.93 and 0.95 (BP86) or 1.010 and 1.030 (B3LYP) for the C_i and C_2 structures, which are consistent with singly occupied SOMO "$34a_g$" or SOMO "32b" orbitals. For the C_i structure, the $34a_g$ orbital is mainly of metallic character (82%), whereas for the C_2 structure the "32b" orbital displays important contributions of 24 and 9% for the Hapac and water ligands, respectively. For both structures obtained with C_i and C_2 symmetries, the Co–$O_1(H_2O)$ bond lengths, which are 2.201 and 2.194 Å (BP86) or 2.175 and 2.169 Å (B3LYP) respectively, are calculated as being slightly longer than the experimental value of 2.149 Å, while the Co–O_3(Hapca) bond distances of 1.940 and 1.950 Å (BP86) or 1.927 and 1.913 Å (B3LYP) are shorter than the experimental one of 2.170 Å. The O_1–Co–O_3 valence angles are 180° in the C_i structure and 83° in the C_2 one, showing the linearity and the bending of the water molecules (Supplementary information), respectively. Furthermore, for the distorted C_2 structure, the dihedral angle between the two Hapca ligands is 89°, showing a perpendicular disposition. While, the oxidized and the reduced structures are less distorted, witnessed by the relatively weak dihedral angle of 66° and 62° (Supplementary information), respectively. The LUMO "$33a_g$" of **[Co]**$^+$ is a crucial orbital and is situated at 1.21 eV higher in energy than the HOMO. This orbital clearly displays antibonding Co–$O_3(H_2O)$ character between the d_z^2 type orbital of the Co atom and the p orbitals of the oxygen atom. The calculated bond distances obtained by the TZ2P basis set are given between brackets in Table 3. The influence on the bond distances is weak, the Co–N distances undergoing a slight increase from 1.930 to 1.999 Å (C_2) and from 1.931 to 1.977 Å (C_i), i.e. changes not exceeding 0.07 Å, the Co–O_3(Hapca) bond distances are slightly shortened by about 0.05 Å, however the Co–$O_1(H_2O)$ bond distances are slightly longer than those obtained by the TZP basis set, going from 1.988 to 2.078 Å (C_2 symmetry), but remain shorter than the experimental ones of 2.170 Å. So, no considerable changes are provided by including a more polarized basis set such as TZ2P.

Calculated natural charges of +1.04 and +1.040 for **[Co]** are obtained for the C_i and C_2 conformers (Supplementary information), respectively. The oxidation of the **[Co]** species gives **[Co]**$^+$ by the detachment of one electron from the SOMO "$34a_g$" singly occupied spin orbital, which is mainly of metallic character (82%), but also displays weak antibonding M–O(Hapca) character. For the oxidized species, the MO diagram shows that the LUMO "$34a_g$" is an antibonding M–$O_1(H_2O)$ orbital, which is in agreement with the shortening of the corresponding bond by the oxidation of

Table 3
Selected parameters for the **[Co]**$^+$, **[Co]**, **[Co]**$^-$ and **[Ni]** complexes. The relative energies ΔE_1 (BP86/TZP) and ΔE_2 (B3LYP/TZP) are given in kcal/mol. Values between parentheses are obtained from B3LYP/TZP calculations. The bold values correspond to the experimental bond distances, while the values between brackets are those obtained by BP86/TZ2P.

Spin state	[Co]$^+$ $S = 0$		[Co] $S = ½$		[Co]$^-$ $S = 0$		[Ni] $S = 0$	
Symmetry	C_2	C_i	C_2	C_i	C_2	C_i	C_2	C_i
ΔE_1	0.0	0.0	9.8	0.0	5.9	0.0	0.0	0.0
ΔE_2	(8.1)	(0.0)	(6.5)	(0.0)	(6.2)	(0.0)	(6.9)	(0.0)
HOMO–LUMO gap	1.51	1.15	–	–	0.39	0.11	1.59	1.69
	(1.77)	(3.06)	–	–	(2.05)	(1.99)	(2.72)	(2.65)
M–N (Å)	1.960	1.950	1.930	1.931	1.874	1.880	1.910	1.899
	[1.972]	[1.953]	[1.999]	[1.977]	[1.873]	[1.910]	[1.898]	[1.898]
	(1.938)	(1.947)	(2.076)	(1.952)	(1.880)	(1.880)	(1.907)	(1.904)
			2.079				**2.079**	
M–O_3 (Å)	1.880	1.920	1.950	1.940	1.945	1.93	1.890	1.876
	[1.916]	[1.896]	[1.984]	[1.922]	[1.940]	(1.947)	[1.889]	[1.873]
	(1.768)	(1.883)	(1.913)	(1.927)	(1.948)	[1.950]	(1.860)	(1.856)
			2.098				**2.043**	
M–O_1 (Å)	2.059	1.980	2.194	2.201	3.421	5.448	4.450	4.840
	[1.186]	[1.976]	[2.199]	[2.214]	[3.412]	(5.945)	[3.509]	[4.807]
	(3.806)	(1.953)	(2.169)	(2.175)	(3.460)		(3.594)	(4.839)
			2.065				**2.053**	

neutral **[Co]**. For the C_i structure, the calculated M–O_1(H_2O) bond distances of 1.980 (BP86) or 1.953 Å (B3LYP) are shorter than those of the neutral **[Co]**, 2.201 (BP86) or 2.175 Å (B3LYP), which are reinforced in the **[Co]**$^+$ species, while the M–O_3(Hapca) bond distances remain almost unchanged. For the oxidized **[Co]**$^+$ species the Co metal acquires a natural charge of +1.204 (C_i) and +1.071 (C_2), showing an enhancement of its oxidation state compared to that of the neutral **[Co]** of +1.044 (C_i) and +1.040 (C_2). The oxidation process corresponds to the Co(II)/Co(III) redox couple, as shown in Scheme 1.

It is worth noting that the isoelectronic **[Fe]**$^-$ and **[Co]** complexes have different molecular structures. For the **[Fe]**$^-$ structure in its singlet and triplet states, the loss of the water molecules can be observed, whereas for the **[Co]** structure, the water molecules are connected to the metal through relatively long Co–O bond distances (Table 3), as discussed previously.

The reduction of the neutral **[Co]**$^-$ species shows the loss of the two water molecules; this can be explained by the orbital analysis. Indeed, population of the 34a_g orbital by a supplementary one electron enhances the Co–O_1(H_2O) antibonding character and thereby causes bonding ruptures, so the H_2O ligands become unconnected to the cobalt atom for the C_i and C_2 structures, giving rise to 16-MVE species with a square-planar geometry (Fig. 4). The reduction process corresponds to the Co(II)/Co(I) redox couple, in agreement with the natural charges of the neutral and the reduced species of +1.04 and +0.69 respectively, thus showing that the metal center has undergone a reduction.

2.4. Nickel complexes

Similarly to the reduced **[Co]**$^-$ species leading to the loss of water molecules, the optimized **[Ni]** structure also does not retain water molecules, while the X-ray characterized structure at low temperature (150 K) [32] showed the connection of two water molecules to the nickel metal with short Ni–O(H_2O) bond lengths of 2.075 Å. These results are reproduced in the polymeric complex of $[AgNi(Hapac)_2(H_2O)_2]^+$ [33], where the Ni ion is hexacoordinated. Additionally, the Ni(II) cation was found to form a $[(Ni(Hapac)_2(H_2O)_2)_2]^{4+}$ dimer linked through hydrogen bonds [34]. However, the optimized geometries in the gas phase with the imposed C_2 and C_i symmetries give rise to idealized square-planar molecular structures with a 16-MVE closed-shell electronic configuration, showing the loss of the two water molecules as obtained for the isoelectronic **[Co]**$^-$ species. The obtained isomer structures were found to be isoenergetic by the BP86 method, but the C_i symmetry structure lies lower in energy than the C_2 one by 6.9 kcal/mol (B3LYP). For the C_i symmetry structure, the calculated Ni–O(Hapca) and Ni–N(Hapca) bond distances are, respectively, 1.876 and 1.899 Å (BP86) or 1.856 and 1.904 Å (B3LYP), which are comparable to those available from experiment, 2.023 and 2.066 Å respectively. The obtained bond distances by TZP deviate slightly from those obtained with the TZ2P basis set, where the differences do not exceed 0.03 Å. Likewise, the obtained parameters for the C_2 symmetry structure are comparable to those of the C_i one. The MO diagram exhibits large HOMO–LUMO gaps of

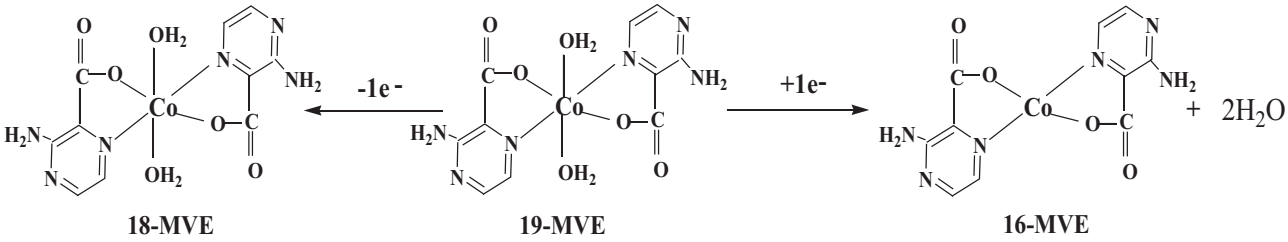

Scheme 1. One-electron oxidation and reduction for the neutral **[Co]** complex of 19-electron configuration.

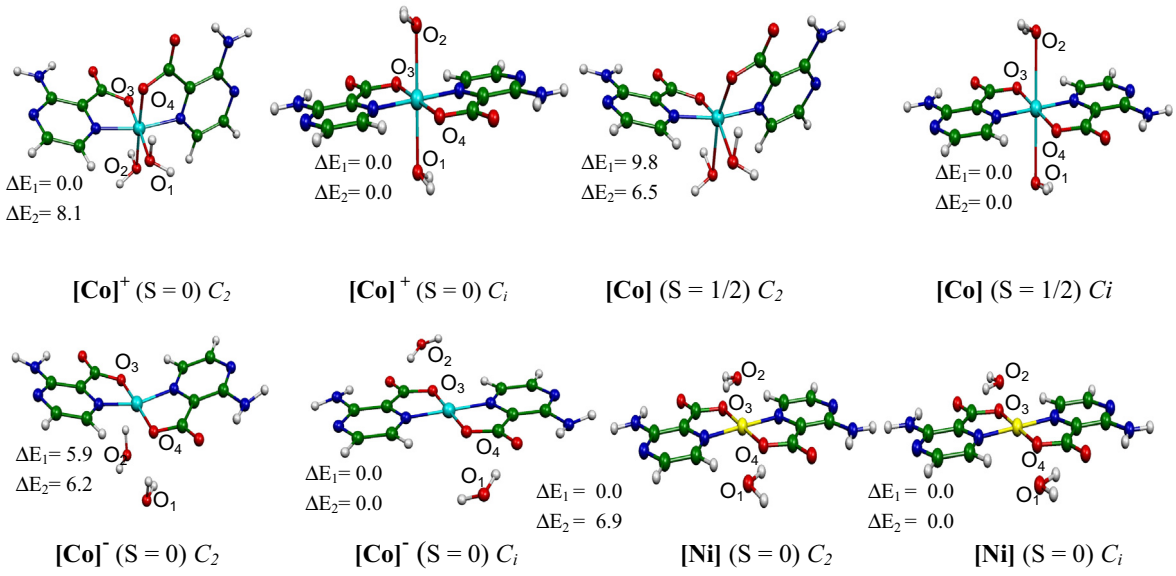

Fig. 4. Optimized **[Co]**$^+$, **[Co]**, **[Co]**$^-$ and **[Ni]** molecular structures of C_i and C_2 symmetries. The relative energies between isomers, ΔE_1 and ΔE_2 (kcal/mol), are obtained by BP86 and B3LYP, respectively.

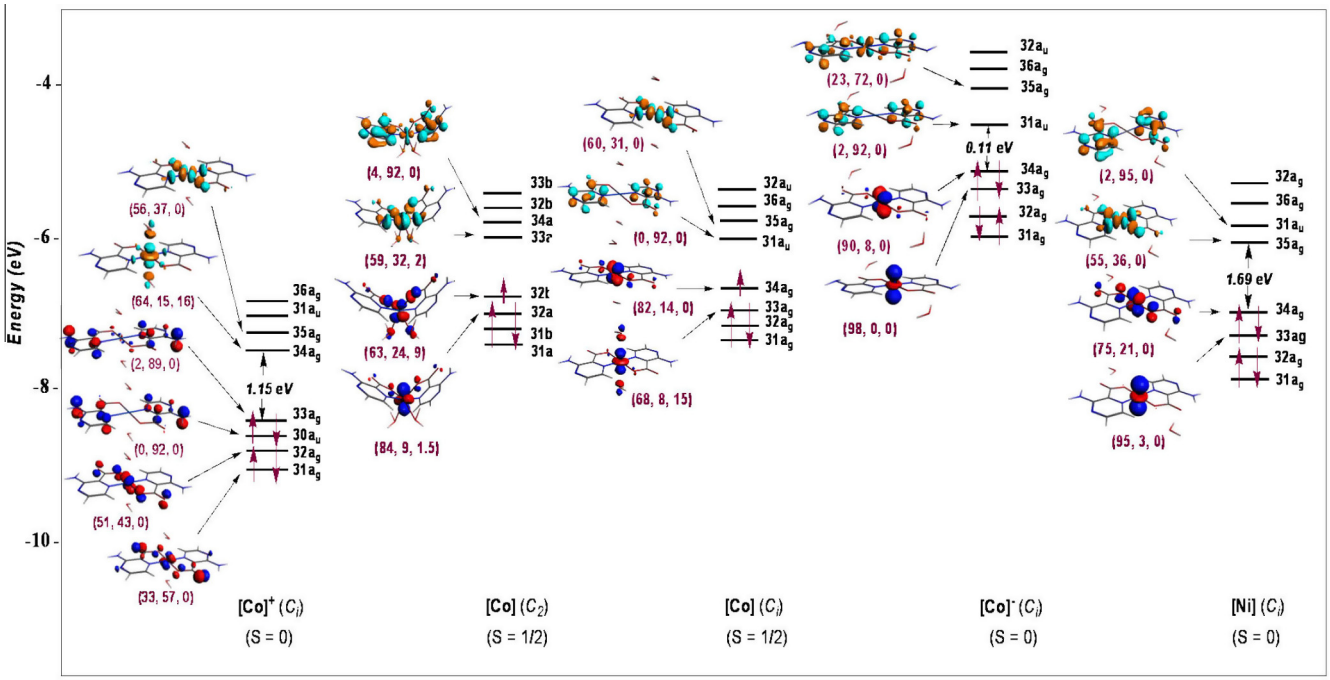

Fig. 5. MO diagrams for **[Co]**$^{+}$ (C_i), **[Co]**$^{-}$ (C_2), **[Co]** (C_i), **[Co]**$^{-}$ (C_i) and **[Ni]** (C_i) structures. Contour plots ±0.06 e/Bohr^3.

1.69 and 1.59 eV (BP86) for the C_i and C_2 structures, respectively, whereas those obtained by B3LYP are much larger, 2.65 and 2.72 eV for the same sequence. The selected structural parameters gathered in Supplementary information show a dihedral $O_1O_2N_1N_2$ angle of 0°, giving rise to a square planar geometry for the Ni(II) d^8 metal environment, in conformity with the molecular planarity, in which the nickel atom acquires a net charge of +1.201 (C_i) and +1.230 (C_2) (see Fig. 5).

2.5. Stability of the oxidized and reduced forms

In order to provide a better insight into the redox properties with respect to their influence on the molecular and electronic structures of the studied complexes, ionization potentials (IPs) and electron affinities (EAs) have been calculated using the BP86 method on the neutral, mono-oxidized and mono-reduced forms of the studied models. The determination of the IPs and EAs is of great importance for an understanding of the thermodynamic and kinetic properties of the investigated complexes.

Vertical ionization potentials (VIP) are calculated by taking the difference between the total energy of the neutral ground state and that of the positively charged complex having a neutral geometry (Table 4). The adiabatic ionization potentials (AIP) are computed as the energy difference between the fully optimized neutral and corresponding anion forms. The vertical electron affinity (VEA) measures the difference in the energy of the neutral complex in its ground state and the corresponding anion complex having the ground state geometry of the neutral complex. On the other hand, the adiabatic electron affinity (AEA) gives the energy difference between the ground states of the neutral and anion forms (Table 4).

The values gathered in Table 4 show that the adiabatic IPs are 0.30–0.82 eV higher in energy than the vertical ones, The general trend of AIP and VIP values obeys the following sequence: Mn < Fe < Co, where the manganese species has the lowest VIP (6.40 eV) and, therefore, is the most easily oxidizable, contrary to the cobalt species with the highest VIP (7.55 eV), thus being the most difficult to oxidize.

The associated energies that occur for electron attachment to form a negative ion are −1.33, −1.69 and −2.75 eV for the Mn, Fe and Co complexes, respectively. The negative AEA values obtained for **[Mn]**$^{-}$, **[Fe]**$^{-}$ and **[Co]**$^{-}$ reduced complexes provide evidence for the existence of anion species. These findings show the ease of reduction for **[Mn]** and **[Fe]** species compared to the

Table 4
Total bonding energies (eV), vertical and adiabatic ionization potentials and adiabatic electron affinities (eV) for Mn, Fe and Co complexes of C_i symmetry obtained by the BP86/TZP basis set.

Complex Spin state	**[Mn]**$^{+}$ (S = 0)	**[Mn]** (S = 0)	**[Mn]**$^{-}$ (S = 1/2)	**[Fe]**$^{+}$ (S = 1/2)	**[Fe]** (S = 0)	**[Fe]**$^{-}$ (S = 1/2)	**[Co]**$^{+}$ (S = 0)	**[Co]** (S = 1/2)	**[Co]**$^{-}$ (S = 0)
Optimized	−224.79	−230.89	−232.22	−223.90	−230.32	−232.01	−222.99	−229.67	−232.43
Single point	−224.49		−231.93	−223.60		−231.83	−222.12		−229.80
Vertical IP	6.40			6.72			7.55		
Adiabatic IP	6.10			6.42			6.68		
Adiabatic EA			−1.33			−1.69			−2.76
			−1.22[a]			−1.51[a]			−2.55[a]
			−1.14[b]			−1.42[b]			−2.39[b]

[a] Adiabatic EA obtained by BP86/QZ3P-1diffuse.
[b] Adiabatic EA obtained by BP86/QZ3P-2diffuse.

predicted difficult reduction of the **[Co]** one. In order to give a deeper insight regarding the influence of the diffuse functions in the basis set on electron affinity, additional calculations have been carried out using QZ3P-*n*diffuse with $n = 1, 2$. The obtained AEAs are gathered in Table 4; one can observe the obvious decrease of the electronic affinity (eV) by using diffuse basis sets. Thus, the one-electron attachment to a neutral species necessitates less energy for yielding anions, as depicted in Table 4. Going from TZP to QZ3P-2diffuse, the AEAs undergo substantial reductions of 0.19, 0.27 and 0.37 eV for the Mn, Fe and Co complexes, respectively, where the AEA of the [Co]/[Co]$^-$ couple is the most affected by including diffuse functions.

3. Computational details

Density functional theory (DFT) calculations were carried out on the studied compounds using the Amsterdam Density Functional (ADF)) program [35], developed by Baerends and co-workers [36–40]. Electron correlation was treated within the local density approximation (LDA) in the Vosko–Wilk–Nusair parametrization [41]. The non-local corrections of Becke and Perdew (BP86) were added to the exchange and correlation energies, respectively [42–44]. Also, geometries have been optimized using the hybrid-type B3LYP functional (Becke's three parameter hybrid exchange functional [45] coupled with the Lee–Yang–Parr non-local correlation functional [46]).

The numerical integration procedure applied for the calculations was developed by te Velde et al. [40]. The atom electronic configurations were described by a triple-ζ Slater-type orbital (STO) basis set for H 1s, C 2s and 2p, N 2s and 2p augmented with a 3d single-ζ polarization for C and N atoms and with a 2p single-ζ polarization for H atoms. A triple-ζ STO basis set was used for the first row transition metals 3d and 4s augmented with a single-ζ 4p polarization function. A frozen-core approximation was used to treat the core shells up to 1s for C, N and 3p for the first row transition metals [36–40]. Full geometry optimizations were carried out using the analytical gradient method implemented by Versluis and Ziegler [47]. Spin-unrestricted calculations were performed for all the open-shell systems. Frequencies calculations [48,49] were performed on all the studied compounds to check that the optimized structures are at local minima on the potential surface of energy. All the energy values reported in this paper include a zero-point energy (ZPE) correction taken out from these frequency calculations. Representation of the molecular structures and molecular orbitals were done using ADF-GUI [35] and MOLEKEL4.1 [50], respectively.

4. Conclusion

Full geometry optimizations of $M(Hapca)_2(H_2O)_2$ complexes showed a good agreement with the available experimental structures. The computed M–O(H_2O) bond lengths are longer than those of M–O(Hapca) ones. The dihedral angle between the two Hapca ligands for the 18-MVE species decreases with respect to the following trend: **[Mn]**$^-$ > **[Fe]** > **[Co]**$^+$. It has been observed that the dihedral angle increases and decreases for the oxidized and reduced species for each metal category, respectively. For all the 18-MVE complexes, the C_2 and C_i symmetries give isoenergetic structures, regardless of the used method. The reduced **[Co]**$^-$ and **[Ni]** structures show the loss of two water molecules, whatever the symmetry and the used method. New structures for oxidized and reduced forms are predicted with various oxidation states in accordance with the considered spin state and the nature of the metal. Several redox couples are highlighted to be in conformity with the oxidized and reduced species as described by the calculated IPs and EAs parameters, where diffuse functions in the basis set decrease sensitively the adiabatic electron affinities (AEAs).

Acknowledgements

The authors are grateful to the Algerian MESRS (Ministère de l'Enseignement Supérieur et de la Recherche Scientifique – Algeria) and to the DGRSDT (Direction Générale de la Recherche Scientifique et du développement Technologique – Algeria) for their financial support.

Appendix A. Supplementary data

Supplementary data associated with this article can be found, in the online version, at http://dx.doi.org/10.1016/j.poly.2014.12.042.

References

[1] A.D. Burrows, C.G. Frost, M.F. Mahon, C. Richardson, Angew. Chem., Int. Ed. 47 (2008) 8482.
[2] A.J. Dobson, R.E. Gerkin, Acta Crystallogr., Sect. C 52 (1996) 1512.
[3] S. Tanase, M. Van Son, A. Gerard, R. Gelder, E. Bouwman, J. Reedijk, Polyhedron 15 (2006) 2967.
[4] S.M. Humphrey, P.T. Wood, J. Am. Chem. Soc. 126 (2004) 13236.
[5] D.M. Ciurtin, M.D. Smith, H.C. zur Loye, Dalton Trans. (2003) 1245
[6] M.L. Tong, X.M. Chen, S.R. Batten, J. Am. Chem. Soc. 125 (2003) 16170.
[7] S.K. Ghosh, P.K. Bharadwaj, Inorg. Chem. 44 (2005) 3156.
[8] J.F. Eubank, R.D. Walsh, M. Eddaoudi, Chem. Commun. (2005) 2095
[9] M.B. Zhang, J. Zhang, S.T. Zheng, G.Y. Yang, Angew. Chem., Int. Ed. 44 (2005) 1385.
[10] J.Y. Lu, Coord. Chem. Rev. 246 (2003) 327.
[11] A. Pawlukojc, I. Natkaniec, Z. Malarski, J. Leciejewicz, J. Mol. Struct. 7 (2000) 516.
[12] S. Gao, S.W. Ng, Acta Crystallogr., Sect. E 66 (2010) m1223.
[13] K.H. Ptasiewicz-Ba, J. Leciejewicz, Pol. J. Chem. 73 (1999) 717.
[14] L. Pan, T. Frydel, M.B. Sander, X. Huang, J. Li, Inorg. Chem. 40 (2001) 1271.
[15] X.M. Zhang, R.Q. Fang, H.S. Wu, S.W. Ng, Acta Crystallogr., Sect. E 60 (2004) m12.
[16] C. Ma, F. Chen, C. Chen, Q. Liu, Acta Crystallogr., Sect. C 59 (2003) m516.
[17] R.-Q. Fang, X.-M. Zhang, Inorg. Chem. 45 (2006) 4801.
[18] V.L. Pecoraro, W.M. Butler, Acta Crystallogr., Sect. C 42 (1986) 1151.
[19] H. Korichi, F. Zouchoune, S.-M. Zendaoui, B. Zouchoune, J.Y. Saillard, Organometallics 29 (2010) 1693.
[20] S. Farah, S. Ababsa, N. Benhamada, B. Zouchoune, Polyhedron 29 (2010) 2722.
[21] N. Bouchakri, A. Benmachiche, B. Zouchoune, Polyhedron 30 (2011) 2644.
[22] A. Benmachiche, S.M. Zendaoui, S.E. Bouaoud, B. Zouchoune, Int. J. Quant. Chem. 113 (2012) 985.
[23] S. Farah, N. Bouchakri, S.M. Zendaoui, J.Y. Saillard, B. Zouchoune, J. Mol. Struct. 953 (2010) 143.
[24] S. Farah, H. Korichi, S.M. Zendaoui, J.Y. Saillard, B. Zouchoune, Inorg. Chim. Acta 362 (2009) 3541.
[25] F. Chekkal, S.M. Zendaoui, B. Zouchoune, J.Y. Saillard, New J. Chem. 37 (2013) 2293.
[26] H. Wang, Y. Xie, R.B. Bruce, H.F. Schaefer III, Eur. J. Inorg. Chem. (2008) 3698
[27] F. Zouchoune, S.M. Zendaoui, N. Bouchakri, A. Djedouani, B. Zouchoune, J. Mol. Struct. 945 (2010) 78.
[28] F. Weinhold, C.R. Landis, Valency and Bonding: A Natural Bond Order Donor-Acceptor Perspective, Cambridge University Press, UK, 2005.
[29] E.D. Glendening, J.K. Badenhoop, A.E. Reed, J.E. Carpenter, J.A. Bohmann, C.M. Morales, F. Weinhold, Theoretical Chemistry Institute, University of Wisconsin, Madison, WI, 2001.
[30] J.C. Rienstra-Kirakofe, G.S. Tschumper, H.F. Schaefer III, Chem. Rev. 102 (2002) 231.
[31] R. Bouchene, S. Bouacida, F. Berrah, R. Belhoues, H. Merazig, Acta Crystallogr., Sect. E 69 (2013) m129.
[32] R. Bouchene, A. Khadri, S. Bouacida, F. Berrah, H. Merazig, Acta Crystallogr., Sect. E 69 (2013) m309.
[33] M. Yang, L.Y. Chai, X.Y. Yi, Acta Crystallogr., Sect. E 68 (2012) m689.
[34] W. Dong, F. Yao, Y.G. Chen, Q. Tang, J. Incl. Macrocycl. Chem. 78 (2013) 397.
[35] ADF2013.01, Theoretical Chemistry, Vrije Universiteit, Amsterdam, The Netherlands, SCM.
[36] E.J. Baerends, D.E. Ellis, P. Ros, Chem. Phys. 2 (1973) 41.
[37] G. te Velde, E.J. Baerends, J. Comput. Phys. 99 (1992) 84.
[38] C. Fonseca Guerra, J.G. Snijders, G. te Velde, E.J. Baerends, Theor. Chim. Acc. 99 (1998) 391.
[39] F.M. Bickelhaupt, E.J. Baerends, Rev. Comput. Chem. 15 (2000) 1.
[40] G. te Velde, F.M. Bickelhaupt, C. Fonseca Guerra, S.J.A. VanGisbergen, E.J. Baerends, J.G. Snijders, T. Ziegler, J. Comput. Chem. 22 (2001) 931.
[41] S.D. Vosko, L. Wilk, M. Nusair, Can. J. Chem. 58 (1990) 1200.

[42] A.D. Becke, J. Chem. Phys. 84 (1986) 4524.
[43] A.D. Becke, Phys. Rev. A. 38 (1988) 3098.
[44] J.P. Perdew, Phys. Rev. B. 33 (1986) 8822.
[45] J.P. Perdew, Phys. Rev. B. 34 (1986) 7406.
[46] A.D. Becke, J. Chem. Phys. 98 (1993) 5648.
[47] L. Versluis, T. Ziegler, J. Chem. Phys. 88 (1988) 322.
[48] L. Fan, T. Ziegler, J. Chem. Phys. 96 (1992) 9005.
[49] L. Fan, T. Ziegler, J. Phys. Chem. 96 (1992) 6937.
[50] P. Flükiger, H.P. Lüthi, S. Portmann, J. Weber, MOLEKEL, Version 4.3.win32, Swiss Center for Scientific Computing (CSCS), Switzerland, 2000–2001. <http://www.cscs.ch/molekel/>.